volume density, thus favouring the formation of molecules. The upper envelope of the MS is populated by cells that, on average, have larger H I surface densities than counterparts located on the relation and below it. Focusing on H_2, we can see that no variations in $\log\Sigma_{H_2}$ are visible perpendicular to the MS relation, while a weak trend on increasing $\log\Sigma_{H_2}$ towards higher $\log\Sigma_{SFR}$ can be seen at fixed stellar surface density. For example, at $\log\Sigma_\star = 7.5$ the average value of $\log\Sigma_{H_2}$ on the MS is 0.8 M$\odot$ pc^{-2}, and increases to $\sim$1.35 M$\odot$ pc^{-2} 0.8 dex above the relation. Following equation (2), this variation in $\log\Sigma_{H_2}$ would correspond to a difference in $\log\Sigma_{SFR}$ of $\sim$0.5 dex, implying that the increase in H_2 seen at fixed stellar surface densities is not sufficient alone in setting large SFR. In the right-hand panels of Fig. 4, we show the distance from the spatially resolved MS plotted as a function of $\log\Sigma_{H\,I}$ (top) and $\log\Sigma_{H_2}$ (bottom). As indicated qualitatively from Fig. 2, we observe a correlation between $\log\Sigma_{H\,I}$ and Δ_{MS}, for which regions located above the MS are characterized by the largest H I surface brightness, while regions below the MS correspond to cells with low $\log\Sigma_{H\,I}$. We do not observe any correlation between $\log\Sigma_{H_2}$ and Δ_{MS}. This is the combination of the two previous results: (1) the molecular KS relation is populated by regions on the MS and (2) the existence of the MGMS. This suggests that the absolute quantity of molecular gas in a region (or, equivalently its surface density) is not related to the sSFR of the region itself.

3.4 Dependence of the results on metallicity

A possible source of uncertainty in this work is the dependence of the conversion factor between CO and H_2 on gas-phase metallicity (α_{CO}). Indeed, several works have shown that α_{CO} varies strongly as a function of the metallicity (e.g. Bolatto et al. 2013), and strong metallicity gradients have been found in some of the galaxies in this sample, as well as in larger samples of local star-forming galaxies (Ho et al. 2014; Chiang et al. 2018; Vílchez et al. 2019), reaching a factor of 10 within the optical radius. From an integrated perspective, instead, Genzel et al. (2015) find that α_{CO} varies little within $\pm$0.6 dex of the MS (thus for the large majority of the cells in this work). Nevertheless, such variations in metallicity need to be addressed properly in order to avoid biased interpretations of spatially resolved results. From the DustPedia archive, we download the table containing all the metallicity measurements available in literature (De Vis et al. 2019) and obtain in regions within R_{25} of the five galaxies in our sample. For NGC 5457, there are 280 estimates of metallicity within the optical radius, while for NGC 6946 only 14 are available. In particular, we make use of the metallicities computed exploiting the N2 and O3N2 calibrations of Pettini & Pagel (2004).[3] In particular, N2 is defined as $\log([\mathrm{N\,II}_{6583A}/\mathrm{H}_\alpha)$ and O3N2 as $\log[([\mathrm{O\,III}]_{5007A}/\mathrm{H}_\beta)/([\mathrm{N\,II}]_{6583A}/\mathrm{H}_\alpha)]$. With the conversion relations of Kewley, Geller & Jansen (2004), we obtain the metallicities in the Denicoló, Terlevich & Terlevich (2002) calibration. For each galaxy, we then build a 1D metallicity profile by fitting the different measurements. We use the 1D metallicity profile to obtain a 2D map of the metallicity dependent α_{CO} factor exploiting the relation of Genzel et al. (2012), that is obtained by fitting the $z \sim 0$ points of Leroy et al. (2011) with $z > 1$ ones collected in Genzel et al. (2012):

$$\log\alpha_{CO} = -1.3 \times (12 + \log(\mathrm{O/H}))_{\mathrm{Denicolo02}} + 12. \quad (5)$$

With the 2D map of $\log\alpha_{CO}$, we then estimate Σ_{H_2}. Fig. 5 shows a comparison of the molecular gas surface density computed considering a constant α_{CO} and the metallicity dependent one (in particular, the one obtained with the O3N2 calibration, but no significant differences are found when considering the N2 one). The highest scatter corresponds to small Σ_{H_2}, located in the outskirts of the optical disc, where the metallicity is, on average, smaller than in the centre. The source characterized by the largest scatter is NGC 5457, that is also the one with the strongest metallicity gradient (Vílchez et al. 2019). We note, nevertheless, that within 0.5 R_{25} (i.e. in first approximation, the distance within which the estimate of Σ_{H_2} is above the sensitivity limit), the maximum difference between the two estimates is around 0.2 dex.

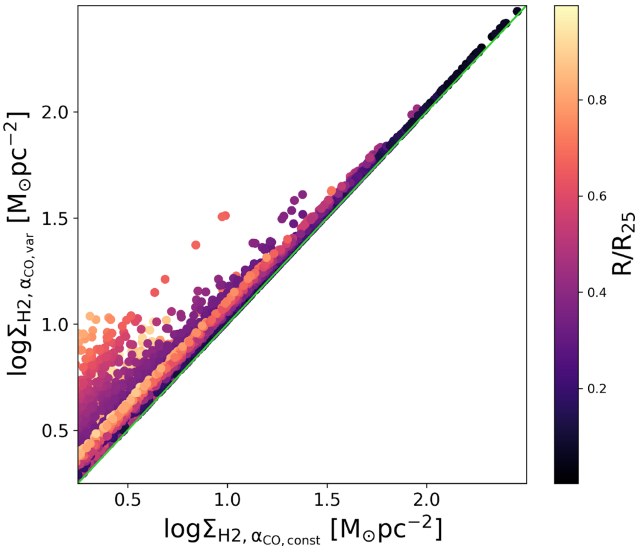

Figure 5. Comparison between the spatially resolved molecular gas mass computed with a constant α_{CO} factor and a metallicity dependent one (here for clarity we use the metallicity based on the O3N2 measurement; no significant differences are found when using the metallicity based on the N2 data). The points are colour coded as a function of their R/R_{25} value. The green solid line marks the 1-to-1 relation.

We repeat the previously shown analysis considering Σ_{H_2} estimated with the metallicity dependent α_{CO}. In Table 2, we report the slopes, intercepts, and scatter of the various relations discussed above: $\log\Sigma_{H_2}$–$\log\Sigma_{SFR}$, $\log\Sigma_{gas}$–$\log\Sigma_{SFR}$, $\log\Sigma_\star$–$\log\Sigma_{H_2}$, and $\log\Sigma_\star$–$\log\Sigma_{gas}$. With respect to the case of constant α_{CO}, the slope of molecular KS relation slightly increases but not significantly given the errors on the estimates. The slope of the total gas KS law decreases to reach values closer to 1, but again this decrease is not significant when taking the errors into account. Similarly, the variations in slope and intercept of the $\log\Sigma_\star$–$\log\Sigma_{H_2,gas}$ relations do not vary significantly with respect to the values found in Section 3.2. The scatter of the four relations slightly increases. In particular, the scatter of the $\log\Sigma_\star$–$\log\Sigma_{H_2,gas}$ relations is comparable or larger than the one of the spatially resolved MS. This is expected, as we are adding several sources of uncertainty: the conversion between different metallicity calibrations, the correlation between α_{CO} and metallicity, as well as the fact that we are averaging the metallicity to obtain a 1D profile. In first approximation, this exercise reveals that the results in this paper are robust against variations of the α_{CO} factor as a function of metallicity, that is the main and most studied dependence of α_{CO} on physical/galaxy properties (e.g. gas temperature and abundance, optical depth, cloud structure, cosmic ray density, and UV radiation field, in addition to the metallicity).

[3]We refer the reader to Casasola et al. (2020) and De Vis et al. (2019) for details of the metallicity calibration.

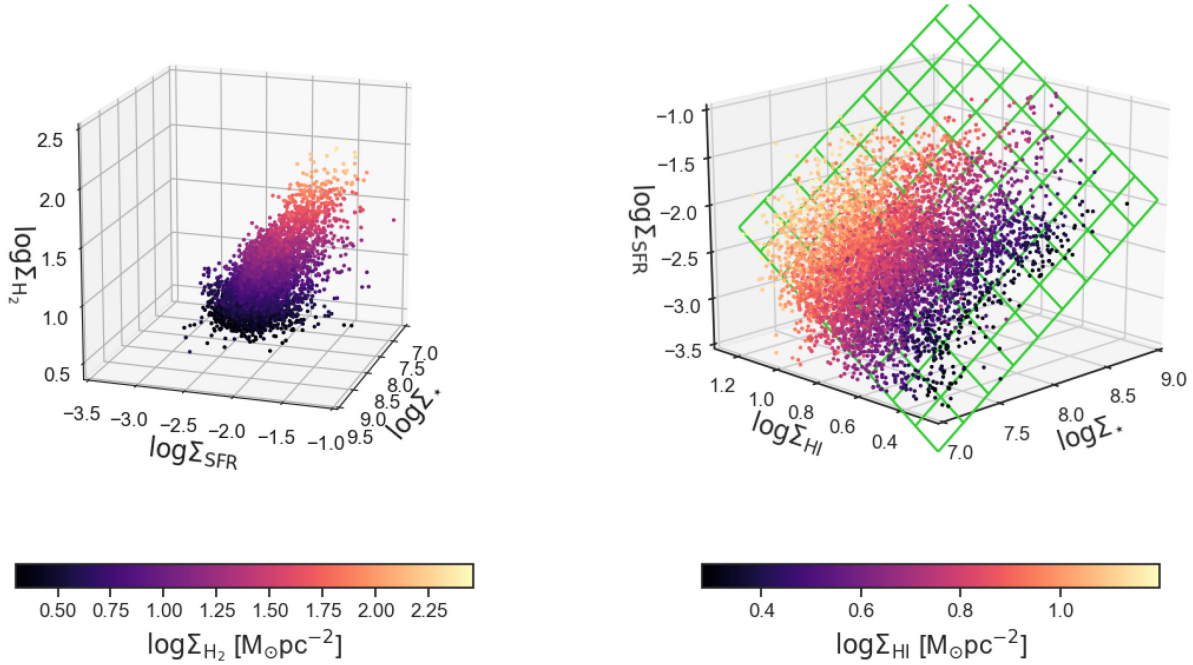

Figure 6. *Left-hand panel*: Distribution of the regions having an estimate of Σ_{H_2} above the sensitivity limit in the log $\Sigma_\star$–log Σ_{SFR} –log Σ_{H_2} plane. Each point is colour coded as a function of log Σ_{H_2}. Four projections of this space at different azimuthal angles are shown in Fig. A1. *Right-hand panel*: Distribution of the regions having an estimate of Σ_{HI} above the sensitivity limit in the log $\Sigma_\star$–log Σ_{SFR}–log Σ_{HI} plane. Each point is colour coded as a function of log Σ_{HI}. The best-fitting plane is indicated by the green grid. Four projections of this plane, described by equation (7), at different azimuthal angles are shown in Fig. A2.

This happens because the central metallicities for the galaxies in our sample are similar, and the molecular gas maps are not deep enough to reach the outermost regions where the metallicity decrease with respect to the central value.

4 DISCUSSION

4.1 The origin of the main sequence and its scatter

The spatially resolved MS of galaxies constitutes the building block of the integrated MS relation of star-forming galaxies, so deeply analysed in literature to understand the star formation processes and the quenching mechanisms. When analysing the molecular gas component of nearby galaxies we find tighter relations than the MS itself, and that may be at the physical origin of it: the KS law (2) and the MGMS (4). By combining equations (2) and (4), we obtain a spatially resolved MS in the form

$$\log \Sigma_{SFR} = 0.73 \times \log \Sigma_\star - 7.89, \quad (6)$$

which, as expected, consistent with the spatially resolved MS relation characterizing our sample (log $\Sigma_{SFR} = 0.76 \log \Sigma_\star - 8.15$, see Section 2.1). We find that the Σ_{H_2}–Σ_{SFR} relation is the tightest one of the three, with a scatter of 0.19 dex, followed by the $\Sigma_\star$–Σ_{H_2} relation, 0.22 dex, similar to the scatter of the spatially resolved MS (0.23 dex). Contrary to Lin et al. (2019), we find that the scatter of the spatially resolved MS is significantly smaller than the quadratic sum of the scatters of the $\Sigma_\star$–Σ_{H_2} and Σ_{H_2}–Σ_{SFR} relations, indicating that the scatters of these relations are not independent. Indeed, regions located in the upper (lower) envelope of the molecular KS relation also populate the upper (lower) envelope of the MGMS. To further investigate the connection between the three relations (KS, MS, MGMS), we plot in the left-hand panel of Fig. 6 how regions with an estimate of Σ_{H_2} above the sensitivity limit populate the 3D space made by log $\Sigma_\star$, log Σ_{SFR}, and log Σ_{H_2} (four different projections of this space are shown in Fig. A1 in Appendix A). The variables define a 3D relation, as found by Lin et al. (2019). This is expected, as we find no dependence of Δ_{MS} on Σ_{H_2} (see Fig. 4). On the other hand, the analysis of Σ_{HI} in the log $\Sigma_\star$–log Σ_{SFR} plane revealed that the spatially resolved MS scatter seems to be connected to the presence of neutral gas. Indeed, when analysing how regions populate the 3D space formed by log $\Sigma_\star$, log Σ_{SFR}, and log Σ_{HI}, we find that they identify a plane, as shown in the right-hand panel of Fig. 6 (four different projections of this plane are shown in Fig. A2 in Appendix A). The equation of the plane that minimizes the perpendicular distance of the points can be written as

$$\log \Sigma_{SFR} = 0.97 \log \Sigma_\star + 1.99 \log \Sigma_{HI} - 11.11. \quad (7)$$

The relation expressed by equation (7) has a scatter of 0.14 dex, significantly smaller than the one of the spatially resolved MS relation. Interestingly, when the dependence of the SFR of H I surface densities is taken into account, the relation between log Σ_{SFR} and log $\Sigma_\star$ becomes closer to linear. To better understand the origin of the relation expressed by equation (7), in Fig. 7 we show the log Σ_{H_2}–log Σ_{HI} plane colour coded as a function of Δ_{MS} (left-hand panel) and r/R_{25} (right-hand panel). From Fig. 7, we can appreciate that regions with Σ_{HI} higher than 10 M$\odot$ pc^{-2} (that is the typical value for the H I to H2 transition, Bigiel et al. 2008; Leroy et al. 2008; Lee et al. 2012, 2014) correspond to the upper envelope of the spatially resolved MS and, on average, are preferentially located between 0.3 and 0.8 R_{25}. These regions span a wide range of log Σ_{H_2} values: (1) up to log Σ_{H_2} = 2 M$_\odot$ pc^{-2} for $0.3R_{25} < r < 0.6\ R_{25}$ and (2) below the sensitivity limit for $r > 0.6\ R_{25}$. In the first case, the stellar surface density and average SFR are moderately high: high H I surface densities could be partially due to H_2 dissociation and are needed (together with dust)

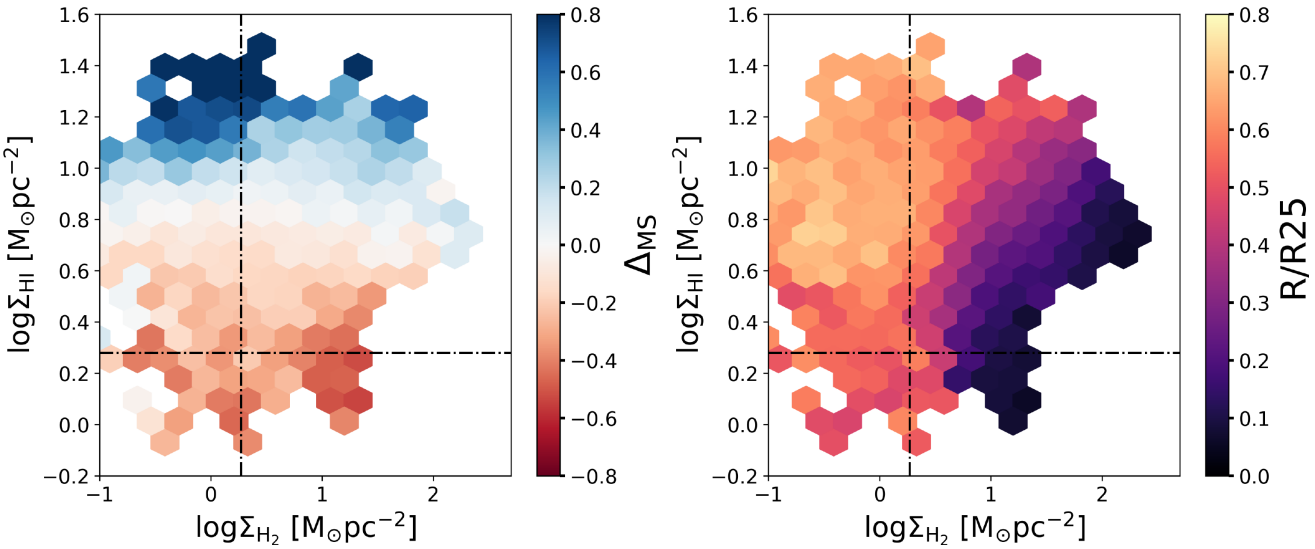

Figure 7. The logΣ_{H_2}–logΣ_{HI} plane, colour coded as a function of Δ_{MS} (left-hand panel) and R/R_{25} (right-hand panel). Sensitivity limits are marked with dot–dashed lines.

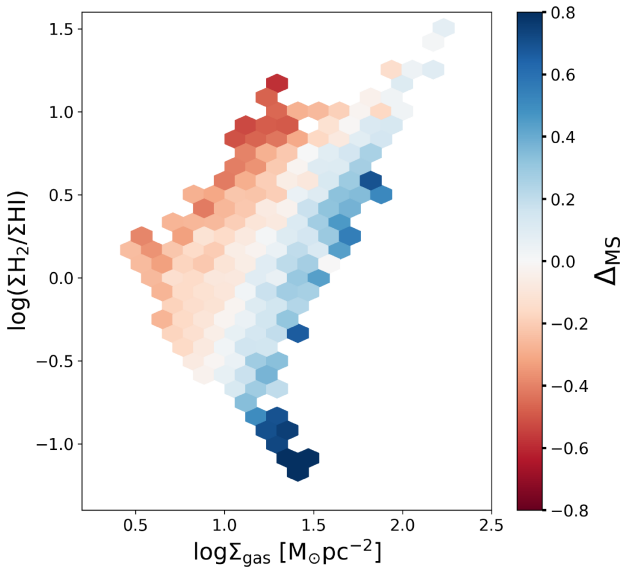

Figure 8. The Σ_{H_2}/Σ_{HI} ratio as a function of Σ_{gas}. The cells have been colour coded as a function of the average Δ_{MS}.

to prevent the further dissociation of the molecular gas by the intense radiation field. In the outer part of the optical disc, the SFRs are on average lower than in the inner disc, and so is the stellar surface density; nevertheless, the SFRs above the MS reach values that are comparable to SFRs on the MS in the inner part of the disc.

Most likely, once the molecular gas gives birth to new stars, it is partly disrupted by the resulting intense UV radiation from hot massive stars. To illustrate this effect, in Fig. 8, we plot the Σ_{H_2}/Σ_{HI} ratio as a function of Σ_{gas}. As expected, for higher Σ_{gas} this ratio increases: H_2 becomes progressively more dominant over H I as the chemical equilibrium shifts in favour of the molecular phase with increasing gas pressure. However, the correlation is quite broad, and the origin of the spread at fixed Σ_{gas} becomes evident once the cells are colour coded as a function of Δ_{MS}. Going from below to above the MS relation, Σ_{H_2}/Σ_{HI} steadily decreases. We interpret this trend as evidence that stellar feedback (radiative and from supernova shocks) has the effect of partially dissociating the H_2 molecules in regions of intense star formation. The sheer size of this trend is worth emphasizing, as the H_2/H I ratio drops by about a factor of 100 when going from extreme sub-MS to super-MS (starbursting) cells. Such a wide range is indeed expected by theory, for a wide variation of the intensity of the UV radiation field (cf. fig. 7 in Sternberg et al. 2014, see also Tacconi, Genzel & Sternberg 2020).

We notice that a correlation between the H I abundance and the distance from the MS has been recently reported by Wang et al. (2020) when analysing integrated galaxy properties; that is, galaxies above the MS are more H I-rich than those below. They interpret this trend in terms of H I being an intermediate step (between the ionized and the molecular phase) in fuelling star formation in galaxies, but do not consider H I as a product of molecular dissociation. Our results instead indicate that H I is also a product of star formation and its surface density is extremely sensitive to the local UV radiation field.

4.2 Star formation efficiency versus gas fraction

The data set in our hands gives us the possibility to analyse the role of SFE and f_{gas} in setting the sSFR of a region, thus deciding its location with respect to the spatially resolved MS relation. As in literature, the gas fraction and SFE estimates may or may not include the contribution of neutral gas, depending on how the gas mass is measured, we define the molecular, atomic, and total SFE: $SFE_{mol} = SFR/M_{H_2}$, $SFE_{ato} = SFR/M_{HI}$, $SFE_{tot} = SFR/(M_{HI}+M_{H_2})$. Similarly, we define the molecular, atomic and total gas fractions as $f_{gas,mol} = M_{H_2}/(M_{H_2}+M_{HI}+M_\star)$, $f_{gas,ato} = M_{HI}/(M_{H_2}+M_{HI}+M_\star)$ and $f_{gas,tot} = (M_{HI}+M_{H_2})/(M_{HI}+M_{H_2}+M_\star)$.

In Fig. 9, we show how the average SFE (top) and f_{gas} (bottom) vary in the log$\Sigma_\star$–logΣ_{SFR} plane, separating the different phases. Qualitatively, we observe that SFE_{mol} varies strongly above and below the MS, for log$\Sigma_\star$ <8 $M_\odot$ kpc^{-2}, while it is almost constant at higher stellar surface densities. These trends reflect the changes in $f_{gas,mol}$, that is characterized by strong variations above/below the MS only at higher stellar surface densities, leading to a constant SFE. We notice that regions above the MS at log$\Sigma_\star$ <7 $M_\odot$ kpc^{-2} have very low $f_{gas,mol}$, as they are located in the outer optical disc. SFE_{ato} (central top panel) is nearly constant above/below the MS,

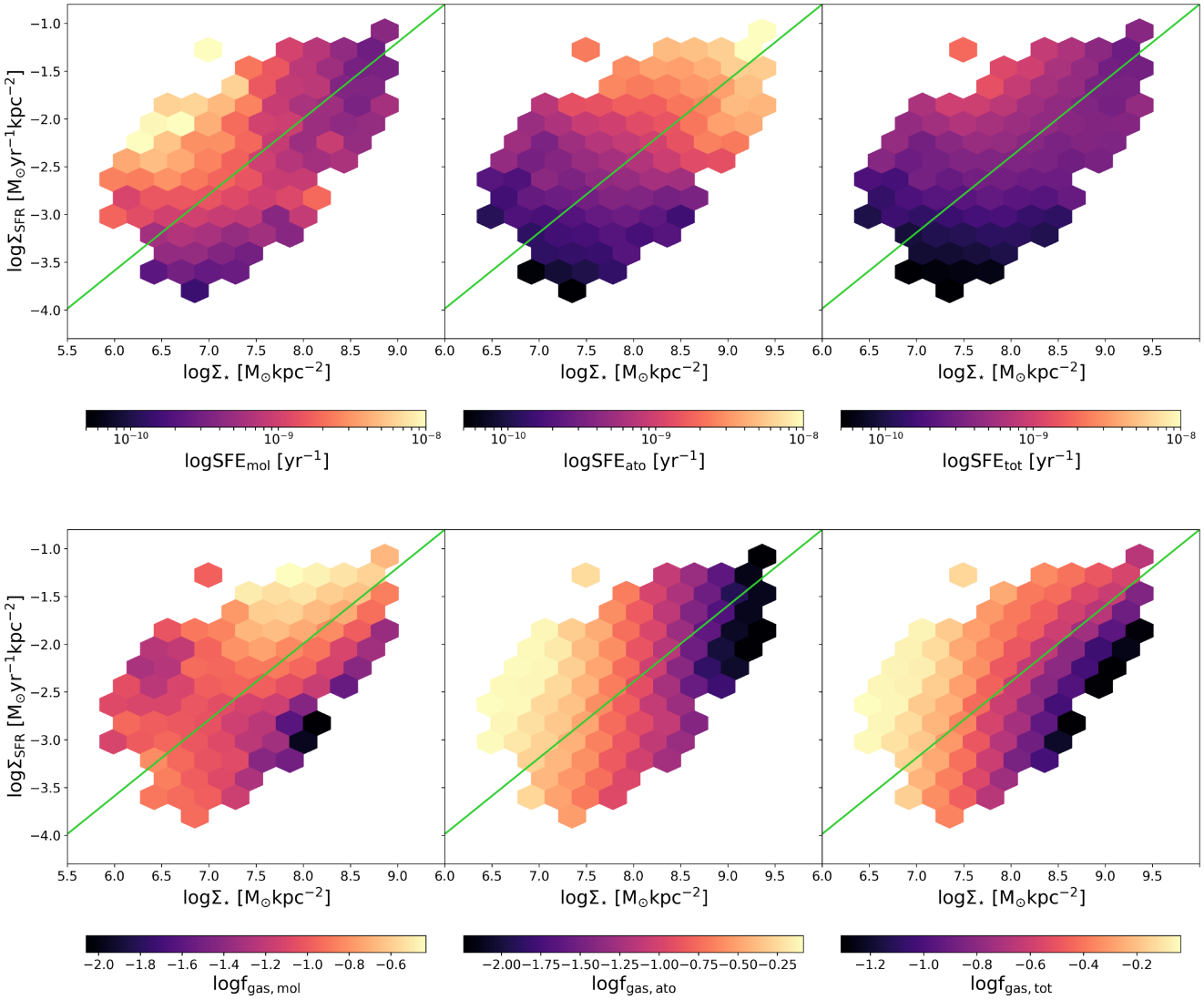

Figure 9. Molecular, atomic, and total SFE and f_{gas} in the $\log\Sigma_\star$–$\log\Sigma_{SFR}$ plane. The bins in the six panels are colour coded as a function of $SFE_{mol} = SFR/M_{H_2}$ in the *top left-hand panel*, $SFE_{ato} = SFR/M_{H1}$ in the *top central panel*, $SFE_{tot} = SFR/(M_{H1}+M_{H_2})$ in the *top right-hand panel*, $f_{gas,mol} = M_{H_2}/(M_{H1}+M_{H_2}+M_\star)$ in the *bottom left-hand panel*, $f_{gas,ato} = M_{H1}/(M_{H1}+M_{H_2}+M_\star)$ in the *bottom central panel*, and $f_{gas,tot} = (M_{H1}+M_{H_2})/(M_{H1}+M_{H_2}+M_\star)$ in the *bottom right-hand panel*. The spatially resolved MS is indicated with the green solid line.

while it steadily increases along the MS relation for increasing stellar surface densities. The atomic gas fraction is subject to two distinct trends: it decreases along the MS relation, from low to high $\Sigma_\star$, and tends to be higher above the MS. When considering the total gas, the variations of SFE_{tot} are less evident: SFE_{tot} increases slightly at fixed stellar surface densities, less significantly in the direction perpendicular to the MS relation, and it increases along the MS for $\log\Sigma_\star < 7.5$ $M_\odot$ kpc^{-2}, to reach an almost constant value for $\log\Sigma_\star > 7.5$ $M_\odot$ kpc^{-2}. Finally, we observe that $f_{gas,tot}$ varies strongly when moving from the lower to the upper envelope of the MS, both perpendicular to the relation and at fixed $\log\Sigma_\star$. Regions with $\log\Sigma_\star < 7.0$ $M_\odot$, that on average correspond to $\log\Sigma_{H_2}$ below the sensitivity limit, have large gas fractions thanks to the contribution of the neutral gas.

The qualitative analysis carried on so far on Fig. 9 points to the role of both the SFE and f_{gas} in regulating the SFR of a region. From an integrated point of view, there is now convergence on the fact that an increase in SFR at fixed $M_\star$ and cosmic epoch is due to a combination of increasing gas mass and decreasing depletion time (thus increasing SFE Saintonge et al. 2011b, 2012; Leroy et al. 2013; Huang & Kauffmann 2014). In the recent years, these studies could be carried out with larger and larger samples, using different sub-mm observations to trace gas, and exploring a wide range of cosmic epochs, $0 < z < 4.5$, with the general consensus that an almost equal increase of gas fraction and SFE can explain an increase in sSFR at fixed redshift. Scoville et al. (2017) exploited sub-mm ALMA continuum observations of 700 COSMOS galaxies at $0.3 < z < 4$ and estimated the gas mass from the dust mass. Several works in literature indicate that the dust mass is a tracer of the total gas mass (e.g. Leroy et al. 2011; Corbelli et al. 2012; Orellana et al. 2017; Casasola et al. 2020), but for $0.3 < z < 4$ the total gas is dominated by the molecular fraction (e.g. Lagos et al. 2014). Genzel et al. (2015) and Tacconi et al. (2018) combine three different estimates of molecular gas mass (from FIR SED, ∼1 mm dust photometry and CO line flux) in the redshift range $0 < z < 4$ and found that an increase in sSFR at fixed stellar mass and redshift is accompanied by an almost equal increase

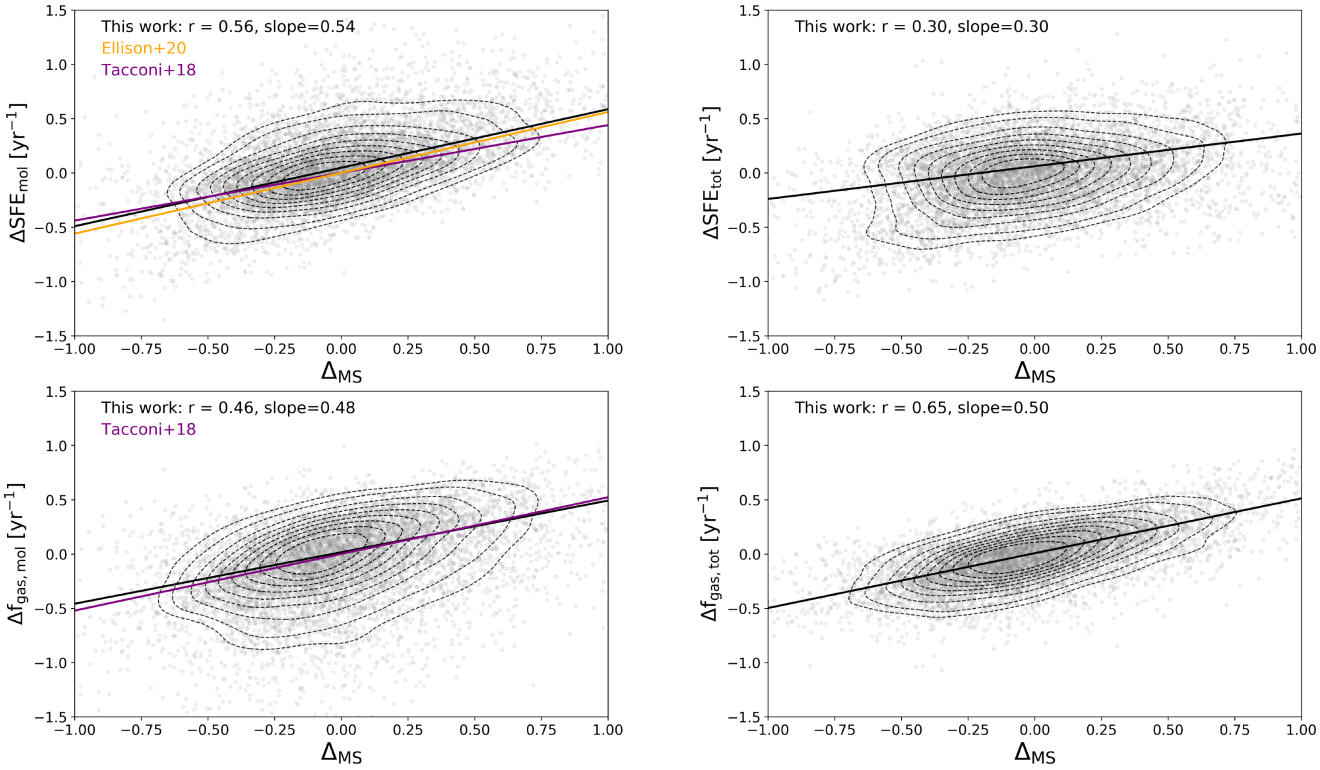

Figure 10. Distributions of regions in the $\Delta_{SFE,mol}$–Δ_{MS} plane (*top left-hand panel*), in the $\Delta_{SFE,tot}$–Δ_{MS} plane (*top right-hand panel*), $\Delta_{f_{gas,mol}}$ –Δ_{MS} plane (*bottom left-hand panel*), and $\Delta_{f_{gas,tot}}$–Δ_{MS} (*bottom right-hand panel*). The best-fitting relations of this work are shown as a black solid line. The best-fitting slope and the Pearson correlation coefficient are witting each panel. In the left-hand panels, we show relations of Tacconi et al. (2018) in purple, and the one of Ellison et al. (2020a) in orange.

of SFE and f_{gas}. Recently, Ellison et al. (2020b), using molecular gas observations from the ALMaQUEST survey (median redshift ∼0.03) on kpc scales, find that variations of the SFE play a major role in setting the SFR at fixed stellar mass (and thus the scatter of the spatially resolved MS), with differences in $f_{gas,mol}$ playing a secondary role. In Fig. 10, we compare our results to the trends found in Tacconi et al. (2018) and Ellison et al. (2020b). We define Δ_{SFE} as the distance of a region from the spatially resolved KS law at fixed molecular gas mass (central panel of Fig. 2), and $\Delta_{f_{gas}}$ as the distance of a region from the spatially resolved MGMS (central panel of Fig. 3), as done in Ellison et al. (2020b). As the analysis of the connection between the scatter of these relations and Δ_{MS} in Sections 3.2 and 3.1 revealed that MS regions are located along the KS and MGMS relations, the definitions of Δ_{SFE} and $\Delta_{f_{gas}}$ given above are consistent with those of Tacconi et al. (2018) that normalize t_{depl} and f_{gas} to their MS values. The panels show the variation between molecular and total SFE and gas fraction of a region with respect to the MS values (thus Δ_{SFE} and $\Delta_{f_{gas}}$) as a function of Δ_{MS}. The top left-hand panel shows the $\Delta_{SFE,mol}$–Δ_{MS} relation; the Pearson correlation coefficient is 0.56 and the best-fitting relation has a slope of 0.54 and a scatter of 0.18 dex, that is in excellent agreement with Tacconi et al. (2018, slope = 0.44) and Ellison et al. (2020b, slope = 0.5). We emphasize here that our work has a spatial resolution of 500 pc, thus reaching surface densities that are ∼1 dex smaller than Ellison et al. (2020b). A similar slope (0.48) is found when analysing $\Delta_{f_{gas,mol}}$ as a function of Δ_{MS}, with a Pearson coefficient of 0.47 and a scatter of 0.23 dex. Our best-fitting relation is in excellent agreement with the one of Tacconi et al. (2018) (obtained from integrated quantities) that has a slope of 0.52. These results emphasize that when analysing the molecular gas phase, an increase in SFR at fixed $M_\star$ and cosmic epoch is due to a combination of increasing gas mass and increasing (decreasing) SFE (t_{depl}). The situation painted by the molecular gas changes when the contribution of neutral gas is taken into account. In the left-hand panels of Fig. 10, we show the $\Delta_{SFE,tot}$–Δ_{MS} (top) and the $\Delta_{f_{gas,tot}}$–Δ_{MS} (bottom) planes, thus considering both the neutral and molecular gas phases. Interestingly, we see that the relation between $\Delta_{SFE,tot}$ and Δ_{MS} is significantly weaker than in the molecular case, as we retrieve a Pearson coefficient of 0.30, a slope of 0.30, and a scatter of 0.28 dex. On the other hand, we observe a stronger correlation between Δ_{MS} and $\Delta_{f_{gas,tot}}$ (Spearman ranking is 0.65), with a slope of 0.50 and a scatter of 0.19 dex. These results indicate the importance of the neutral gas phase in setting the scatter of the spatially resolved MS, as it partially traces molecular gas dissociated by the radiation field.

Finally, the data set in our hands allows us to analyse the spatial variations of SFE and f_{gas} within the five galaxies of the sample. The spatially resolved maps of Δ_{MS}, $\Delta_{SFE,tot}$, and $\Delta_{f_{gas,tot}}$ for every galaxy can be found in Appendix B (Figs B1 and B2). Here, we emphasize that while we do observe variations within galaxies and among them of the connection between Δ_{MS} and f_{gas} or SFE, on average the galaxy-by-galaxy analysis confirms that the gas fraction strongly correlates with Δ_{MS}.

5 CONCLUSIONS

In this manuscript, we exploit the combination of highly accurate measurements of $\Sigma_\star$ and Σ_{SFR} at 500 pc resolution of five nearby, face-on spiral galaxies obtained following the procedure presented in Paper I, with observations of neutral and molecular gas. With this powerful data set, we study how the location of a region with respect

to the spatially resolved main sequence (MS) is related to the gas in the different phases. We summarize here our main results:

(i) We find that $\log \Sigma_\star$, $\log \Sigma_{\rm SFR}$, and $\log \Sigma_{\rm H_2}$ define a 3D relation (the left-hand panel of Fig. 6); the three projections are the Kennicutt–Schmidt (KS) law, the MS, and the molecular gas main sequence (MGMS). The KS law is the tightest relation, with a scatter of 0.19 dex, followed by the MGMS (0.22 dex) and the spatially resolved MS (0.23 dex). The existence of the MGMS at sub-kpc scales opens up the possibility to study molecular gas content from $\log\Sigma_{\rm SFR}$ and $\log\Sigma_\star$ alone, which are generally easier to obtain and available for large samples.

(ii) We study the distribution of the neutral and molecular gas in the $\log\Sigma_\star$–$\log\Sigma_{\rm SFR}$ plane (Fig. 4) and we find that the surface density of molecular gas steadily increases along the MS relation, but is almost constant perpendicular to it. The surface density of neutral gas, instead, is almost constant along the MS, and increases (decreases) in its upper (lower) envelope. On average, regions located in the upper envelope of the spatially resolved MS have $\Sigma_{\rm H\,I} \geq 10\ {\rm M_\odot\ pc^{-2}}$, that is the typical value for the H I to H_2 transition. The three variables $\log \Sigma_\star$, $\log \Sigma_{\rm SFR}$, and $\log \Sigma_{\rm H\,I}$ are distributed along the plane $\log \Sigma_{\rm SFR} = 0.97 \log \Sigma_\star + 1.99 \log \Sigma_{\rm H\,I} - 11.11$ that has a scatter of 0.14 dex (the right-hand panel of Fig. 6).

(iii) When moving towards high $\Sigma_{\rm SFR}$ at fixed stellar surface densities, the molecular gas fraction and molecular SFE both increase. On the other hand, when we consider the total gas, thus also the contribution of the neutral component, we observe a steep increase of the gas fraction towards high SFRs, accompanied by a weak increase of the total SFE (Fig. 10).

Our results illustrate the intricate interplay between neutral and molecular gas, as it changes radially as a function of the distance from the centre of galaxies, as well as locally depending on the sSFR. We argue that molecular gas dissociation plays an important role in setting the observed trends of neutral and molecular gas surface densities around the MS relation (Fig. 8). Thus, high total gas surface densities favour the formation of molecular hydrogen clouds, which in turn promote star formation whose resulting UV radiation has the effect of dissociating the molecules, in a local baryon cycle that is a manifestation of the self-regulating nature of the star formation process. We shall return on these issues in a future paper, also expanding on their implications for our understanding of the star-formation process in high-redshift galaxies. These trends, obtained here for massive, disc-dominated spirals without a strong bar, will be analysed for galaxies with different morphologies (bulge dominated and spirals with strong bars) in another upcoming paper.

The continuity of trends above the MS, MGMS, and KS relations suggests that starburst regions do not result from a bi-modality in the star formation process, but rather from a steady variation of primarily the total gas fraction and partially the star formation efficiency. We speculate that this continuity could also explain the existence of high redshift starbursts, as the scatter of the spatially resolved MS is similar to the one of the integrated relation, and this last quantity is observed to be constant with redshift. It is widely believed that high-redshift galaxies are dominated by H_2 over H I, because their higher gas surface density favours the molecular phase. However, this finding suggests that the higher sSFR at high redshift may actually contrast this expectation, with intense stellar feedback leading to dissociation thus reducing the H_2/H I ratio. The next generation of radio telescopes like the $_{\rm Square}$ Kilometer Array (SKA), also ongoing surveys with MeerKAT, such as MIGHTEE (Jarvis et al. 2016) and LADUMA (Blyth et al. 2016), will directly measure the H I content in distant galaxies, thus unravelling its role in the star formation processes at earlier cosmic epochs.

ACKNOWLEDGEMENTS

We thank the anonymous referee for constructive comments that improved the manuscript. LM is grateful to Sara Ellison and Bhaskar Agarwal for helpful discussion on the manuscript. LM acknowledges support from the BIRD 2018 research grant from the ⟨0:funding-source 3:href="http://dx.doi.org/10.13039/501100003500"⟩Università degli Studi di Padova⟨/0:funding-source⟩. AE and GR are supported from the STARS@UniPD grant. GR acknowledges the support from grant PRIN MIUR 2017 – 20173ML3WW_001. GR and CM acknowledge funding from the INAF PRIN-SKA 2017 programme 1.05.01.88.04. We acknowledge funding from the INAF main stream 2018 programme 'Gas-DustPedia: A definitive view of the ISM in the Local Universe'. This research made use of PHOTUTILS, an ASTROPY package for detection and photometry of astronomical sources (Bradley et al. 2019).

DATA AVAILABILITY

This research is based on observations made with the Galaxy Evolution Explorer, obtained from the MAST data archive at the Space Telescope Science Institute, which is operated by the Association of Universities for Research in Astronomy, Inc., under NASA contract NASA 5-26555. This work made use of HERACLES, 'The HERACO-Line Extragalactic Survey' (Leroy et al. 2009), and THINGS, 'The H I Nearby Galaxy Survey' (Walter et al. 2008). DustPedia is a collaborative focused research project supported by the European Union under the Seventh Framework Programme (2007–2013) call (proposal no. 606847). The participating institutions are Cardiff University, UK; National Observatory of Athens, Greece; Ghent University, Belgium; Université Paris Sud, France; National Institute for Astrophysics, Italy and CEA (Paris), France. We acknowledge the usage of the HyperLeda database (http://leda.univ-lyon1.fr). The derived data underlying this article will be shared on reasonable request to the corresponding author.

REFERENCES

Abdurro'uf, Akiyama M., 2017, MNRAS, 469, 2806
Barrera-Ballesteros J. K. et al., 2020, MNRAS, 492, 2651
Bell E. F., Kennicutt Robert C. J., 2001, ApJ, 548, 681
Bigiel F., Leroy A., Walter F., Brinks E., de Blok W. J. G., Madore B., Thornley M. D., 2008, AJ, 136, 2846
Bigiel F., Leroy A., Walter F., Blitz L., Brinks E., de Blok W. J. G., Madore B., 2010, AJ, 140, 1194
Blitz L., Rosolowsky E., 2006, ApJ, 650, 933
Bluck A. F. L., Maiolino R., Sánchez S. F., Ellison S. L., Thorp M. D., Piotrowska J. M., Teimoorinia H., Bundy K. A., 2020, MNRAS, 492, 96
Blyth S. et al., 2016, in MeerKAT Science: On the Pathway to the SKA. p. 4
Boissier S., Prantzos N., Boselli A., Gavazzi G., 2003, MNRAS, 346, 1215
Bolatto A. D. et al., 2017, ApJ, 846, 159
Bolatto A. D., Wolfire M., Leroy A. K., 2013, ARA&A, 51, 207
Bouché N. et al., 2010, ApJ, 718, 1001
Bradley L. et al., 2019, astropy/photutils: v0.6
Brinchmann J., Charlot S., White S. D. M., Tremonti C., Kauffmann G., Heckman T., Brinkmann J., 2004, MNRAS, 351, 1151
Bundy K. et al., 2015, ApJ, 798, 7
Cano-Díaz M. et al., 2016, ApJ, 821, L26
Cano-Díaz M., Ávila-Reese V., Sánchez S. F., Hernández-Toledo H. M., Rodríguez-Puebla A., Boquien M., Ibarra-Medel H., 2019, MNRAS, 488, 3929
Casasola V. et al., 2017, A&A, 605, A18
Casasola V. et al., 2020, A&A, 633, A100
Casasola V., Hunt L., Combes F., García-Burillo S., 2015, A&A, 577, A135
Chabrier G., 2003, PASP, 115, 763

Chiang I. D., Sandstrom K. M., Chastenet J., Johnson L. C., Leroy A. K., Utomo D., 2018, ApJ, 865, 117
Clark C. J. R. et al., 2018, A&A, 609, A37
Corbelli E. et al., 2012, A&A, 542, A32
Corbelli E. et al., 2017, A&A, 601, A146
da Cunha E., Charlot S., Elbaz D., 2008, MNRAS, 388, 1595
Daddi E. et al., 2007, ApJ, 670, 156
Daddi E. et al., 2010, ApJ, 714, L118
Davies J. I. et al., 2017, PASP, 129, 044102
de los Reyes M. A. C., Kennicutt Robert C. J., 2019, ApJ, 872, 16
De Vis P. et al., 2019, A&A, 623, A5
Dekel A. et al., 2009, Nature, 457, 451
Denicoló G., Terlevich R., Terlevich E., 2002, MNRAS, 330, 69
Dey B. et al., 2019, MNRAS, 488, 1926
Elbaz D. et al., 2007, A&A, 468, 33
Ellison S. L., Thorp M. D., Pan H.-A., Lin L., Scudder J. M., Bluck A. F. L., Sánchez S. F., Sargent M., 2020a, MNRAS, 492, 6027
Ellison S. L. et al., 2020b, MNRAS, 493, L39
Elmegreen B. G., 1993, ApJ, 411, 170
Enia A. et al., 2020, MNRAS, 493, 4107 (Paper I)
Ford G. P. et al., 2013, ApJ, 769, 55
Foreman-Mackey D., Hogg D. W., Lang D., Goodman J., 2013, PASP, 125, 306
Freundlich J. et al., 2013, A&A, 553, A130
Freundlich J. et al., 2019, A&A, 622, A105
Genzel R. et al., 2010, MNRAS, 407, 2091
Genzel R. et al., 2011, ApJ, 733, 101
Genzel R. et al., 2012, ApJ, 746, 69
Genzel R. et al., 2013, ApJ, 773, 68
Genzel R. et al., 2015, ApJ, 800, 20
Hall C., Courteau S., Jarrett T., Cluver M., Meurer G., Carignan C., Audcent-Ross F., 2018, ApJ, 865, 154
Ho I. T. et al., 2014, MNRAS, 444, 3894
Hopkins P. F., Kereš D., Oñorbe J., Faucher-Giguère C.-A., Quataert E., Murray N., Bullock J. S., 2014, MNRAS, 445, 581
Hsieh B. C. et al., 2017, ApJ, 851, L24
Huang M.-L., Kauffmann G., 2014, MNRAS, 443, 1329
Jarvis M. et al., 2016, in Proceedings of MeerKAT Science: On the Pathway to the SKA. 25-27 May, 2016 Stellenbosch, South Africa (MeerKAT2016). p. 6, Online at: https://pos.sissa.it/cgi-bin/reader/conf.cgi?confid=277
Kashino D. et al., 2013, ApJ, 777, L8
Kennicutt Robert C. J., 1998, ApJ, 498, 541
Kennicutt R. C., Evans N. J., 2012, ARA&A, 50, 531
Kewley L. J., Geller M. J., Jansen R. A., 2004, AJ, 127, 2002
Kruijssen J. M. D. et al., 2019, Nature, 569, 519
Krumholz M. R., McKee C. F., 2005, ApJ, 630, 250
Krumholz M. R., Dekel A., McKee C. F., 2012, ApJ, 745, 69
Kumari N., Irwin M. J., James B. L., 2020, A&A, 634, A24
Kurczynski P. et al., 2016, ApJ, 820, L1
Lagos C. d. P., Davis T. A., Lacey C. G., Zwaan M. A., Baugh C. M., Gonzalez-Perez V., Padilla N. D., 2014, MNRAS, 443, 1002
Lee N. et al., 2017, MNRAS, 471, 2124
Lee M.-Y. et al., 2012, ApJ, 748, 75
Lee M.-Y., Stanimirović S., Wolfire M. G., Shetty R., Glover S. C. O., Molina F. Z., Klessen R. S., 2014, ApJ, 784, 80
Leroy A. K. et al., 2009, AJ, 137, 4670
Leroy A. K. et al., 2011, ApJ, 737, 12
Leroy A. K. et al., 2013, AJ, 146, 19
Leroy A. K., Walter F., Brinks E., Bigiel F., de Blok W. J. G., Madore B., Thornley M. D., 2008, AJ, 136, 2782
Lilly S. J., Carollo C. M., Pipino A., Renzini A., Peng Y., 2013, ApJ, 772, 119
Lin L. et al., 2017, ApJ, 851, 18
Lin L. et al., 2019, ApJ, 884, L33
Makarov D., Prugniel P., Terekhova N., Courtois H., Vauglin I., 2014, A&A, 570, A13
Medling A. M. et al., 2018, MNRAS, 475, 5194
Mihos J. C., Harding P., Spengler C. E., Rudick C. S., Feldmeier J. J., 2013, ApJ, 762, 82
Morselli L., Popesso P., Cibinel A., Oesch P. A., Montes M., Atek H., Illingworth G. D., Holden B., 2019, A&A, 626, A61
Noeske K. G. et al., 2007, ApJ, 660, L47
Orellana G. et al., 2017, A&A, 602, A68
Orr M. E. et al., 2018, MNRAS, 478, 3653
Pearson W. J. et al., 2018, A&A, 615, A146
Peng Y.-j., Renzini A., 2020, MNRAS, 491, L51
Pettini M., Pagel B. E. J., 2004, MNRAS, 348, L59
Planck Collaboration XIII, 2016, A&A, 594, A13
Popesso P. et al., 2019, MNRAS, 483, 3213
Rodighiero G. et al., 2011, ApJ, 739, L40
Roychowdhury S., Huang M.-L., Kauffmann G., Wang J., Chengalur J. N., 2015, MNRAS, 449, 3700
Saintonge A. et al., 2011a, MNRAS, 415, 32
Saintonge A. et al., 2011b, MNRAS, 415, 61
Saintonge A. et al., 2012, ApJ, 758, 73
Salim S. et al., 2007, ApJS, 173, 267
Santini P. et al., 2017, ApJ, 847, 76
Schmidt M., 1959, ApJ, 129, 243
Schreiber C. et al., 2015, A&A, 575, A74
Schruba A. et al., 2011, AJ, 142, 37
Scoville N. et al., 2017, ApJ, 837, 150
Shetty R., Kelly B. C., Bigiel F., 2013, MNRAS, 430, 288
Shetty R., Kelly B. C., Rahman N., Bigiel F., Bolatto A. D., Clark P. C., Klessen R. S., Konstandin L. K., 2014a, MNRAS, 437, L61
Shetty R., Clark P. C., Klessen R. S., 2014b, MNRAS, 442, 2208
Shi Y. et al., 2018, ApJ, 853, 149
Shi Y., Helou G., Yan L., Armus L., Wu Y., Papovich C., Stierwalt S., 2011, ApJ, 733, 87
Silverman J. D. et al., 2015, ApJ, 812, L23
Silverman J. D. et al., 2018, ApJ, 867, 92
Solomon P. M., Downes D., Radford S. J. E., Barrett J. W., 1997, ApJ, 478, 144
Speagle J. S., Steinhardt C. L., Capak P. L., Silverman J. D., 2014, The Astrophysical Journal Supplement Series, 214, 15
Springel V., Hernquist L., 2003, MNRAS, 339, 312
Sternberg A., Le Petit F., Roueff E., Le Bourlot J., 2014, ApJ, 790, 10
Swaters R. A., van Albada T. S., van der Hulst J. M., Sancisi R., 2002, A&A, 390, 829
Tacchella S., Dekel A., Carollo C. M., Ceverino D., DeGraf C., Lapiner S., Mand elker N., Primack Joel R., 2016, MNRAS, 457, 2790
Tacconi L. J. et al., 2010, Nature, 463, 781
Tacconi L. J. et al., 2013, ApJ, 768, 74
Tacconi L. J. et al., 2018, ApJ, 853, 179
Tacconi L. J., Genzel R., Sternberg A., 2020, preprint (arXiv:2003.06245)
Tan J. C., 2000, ApJ, 536, 173
Vílchez J. M., Relaño M., Kennicutt R., De Looze I., Mollá M., Galametz M., 2019, MNRAS, 483, 4968
Vulcani B. et al., 2019, MNRAS, 488, 1597
Walter F., Brinks E., de Blok W. J. G., Bigiel F., Kennicutt Robert C. J., Thornley M. D., Leroy A., 2008, AJ, 136, 2563
Wang J. et al., 2013, MNRAS, 433, 270
Wang J., Catinella B., Saintonge A., Pan Z., Serra P., Shao L., 2020, ApJ, 890, 63
Whitaker K. E., van Dokkum P. G., Brammer G., Franx M., 2012, ApJ, 754, L29
Wyder T. K. et al., 2009, ApJ, 696, 1834

SUPPORTING INFORMATION

Supplementary data are available at *MNRAS* online.

FigureA1_animated.mp4
FigureA2_animated.mp4

Please note: Oxford University Press is not responsible for the content or functionality of any supporting materials supplied by the authors. Any queries (other than missing material) should be directed to the corresponding author for the article.

APPENDIX A: THE LOG $\Sigma_\star$–LOG Σ_{SFR}–log $\Sigma_{H_2,HI}$ 3D RELATION

As shown in Fig. 6, the three quantities log $\Sigma_\star$, log Σ_{SFR}, and log Σ_{H_2} define a 3D relation. To better visualize this relation, in Fig. A1 we show four different projections of it, corresponding to azimuthal angles of 0°, 60°, 120°, and 180°. We stress here that we are plotting only the regions that have an estimate of Σ_{H_2} above the sensitivity limit. In Fig. A2, we show, instead, the log $\Sigma_\star$, log Σ_{SFR}, and log Σ_{HI} 3D plane at four different azimuthal angles, with the aim of better visualize the positioning of the cells along the 3D plane marked in green. We plot in Fig. A2 only the regions that have an estimate of Σ_{HI} above the sensitivity limit.

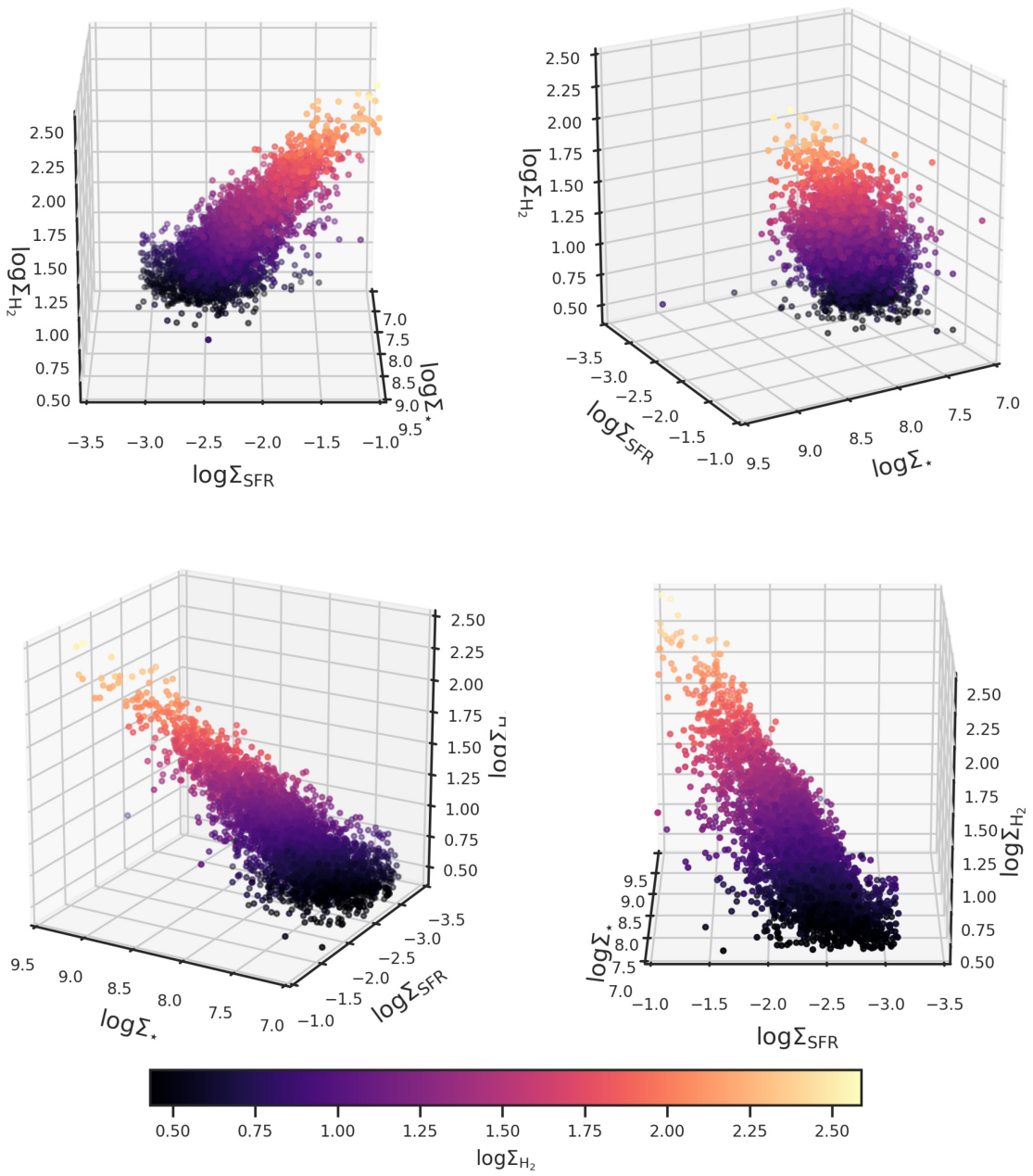

Figure A1. Distribution of the regions with an estimate of log Σ_{H_2} above the sensitivity limit in the log $\Sigma_\star$–log Σ_{SFR}–log Σ_{H_2} 3D space. For different projections of the plane are shown, corresponding to different azimuthal angles: 0° (top left), 60° (top right), 120° (bottom left), and 180 ° (bottom right). The point are colour coded as a function of log Σ_{HI}.

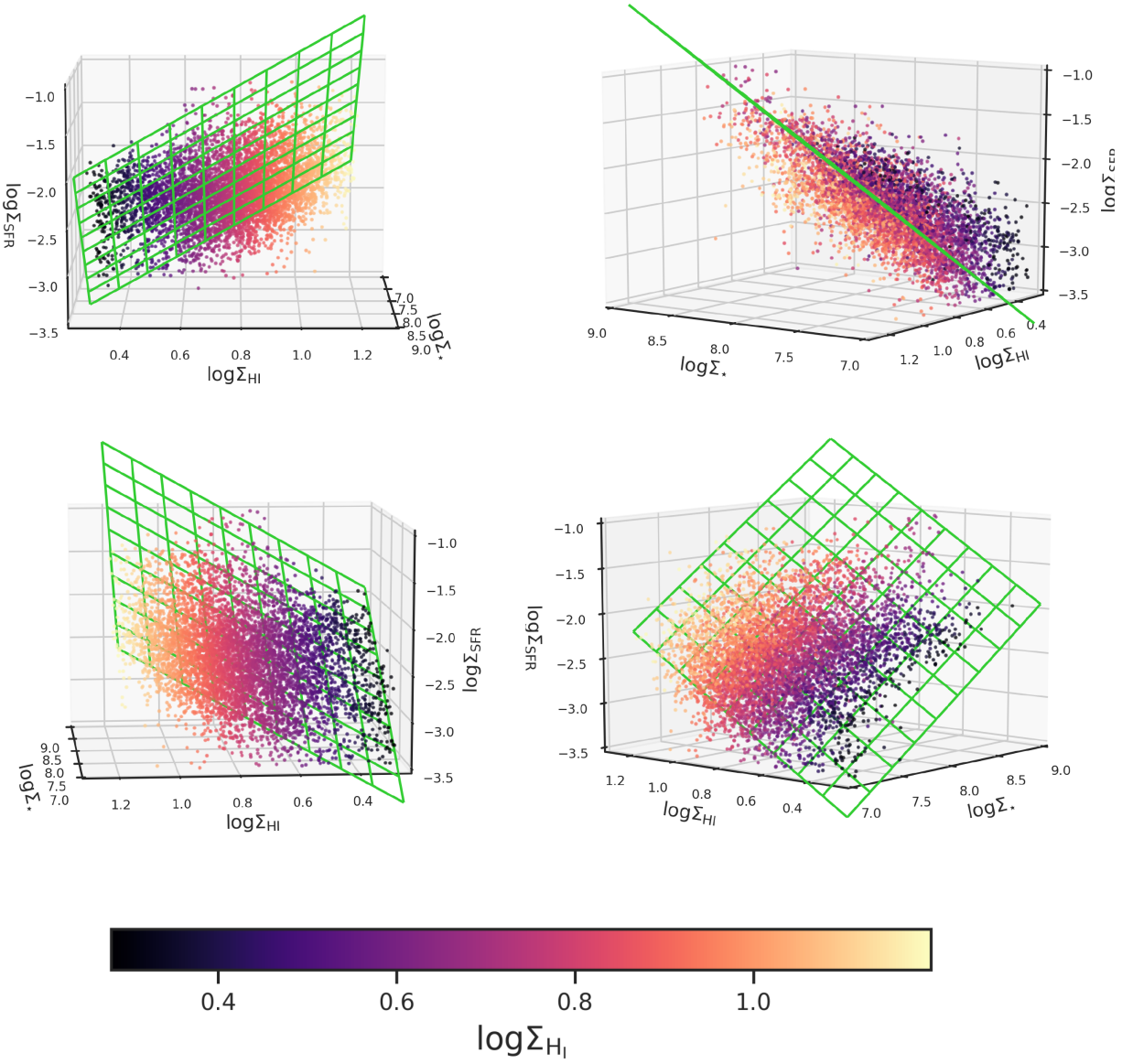

Figure A2. Distribution of the regions with an estimate of log $\Sigma_{\rm H\,I}$ above the sensitivity limit in the log $\Sigma_\star$–log $\Sigma_{\rm SFR}$–log $\Sigma_{\rm H_I}$ 3D space. For different projections of the plane are shown, corresponding to different azimuthal angles: 0° (top left), 125° (top right), 175° (bottom left), and 220 ° (bottom right). The points are colour coded as a function of log $\Sigma_{\rm H_2}$.

APPENDIX B: $\Delta_{\rm MS}$, SFE, AND GAS CONTENT WITHIN GALAXIES

In this section, we discuss the distributions of $\Delta_{\rm MS}$, $\Delta_{\rm f_{gas,tot}}$, and $\Delta_{\rm SFE,tot}$ within the five galaxies in our sample, shown in Figs B1 and B2. We recall here that $\Delta_{\rm SFE,tot}$ and $\Delta_{\rm f_{gas,tot}}$ are computed as the distance of the region from the global total gas–SFR relation (the right-hand panel of Fig. 2) and from the global total gas–mass relation (the right-hand panel of Fig. 3), and are thus a measure of the SFE and gas content with respect to the value on the best-fitted relation at a given gas or stellar surface density (e.g. regions with $\Delta_{\rm f_{gas,tot}} > 0$ have higher gas content than the average).

It is clear that the $\Delta_{\rm SFE,tot}$ and the $\Delta_{\rm f_{gas,tot}}$ in the inner regions will be anticorrelated because the regions where the bulk of molecular hydrogen is not spatially coincident with the regions where the FUV star formation tracer peaks. This is due to the time-delay between the formation of molecular clouds and the exposed phase of star formation (Corbelli et al. 2017). In the inner regions of spiral galaxies, the spiral pattern rotates slower than the stars and hence molecular clouds form out of compressed gas along the inner part of the arm. These are the regions with higher gas fraction than the average. The young stars become visible after dispersing the original gas and, moving faster than the arm, they appear shifted with respect to the newly formed molecular complexes. These are regions with low gas content but numerous visible young stars, hence appear with a star formation efficiency above the average. For the outer regions, at or beyond corotation, the situation should reverse with respect to the arm but the anticorrelation between $\Delta_{\rm SFE,tot}$ and the $\Delta_{\rm f_{gas,tot}}$ should still hold. Here, the low surface density of molecules and the presence of external perturbations make the study more challenging: tidal perturbations, gas stripping, and infall have a strong impact and this reflects on $\Delta_{\rm MS}$ that can vary substantially from one region to the next, being star-forming regions more coarsely spaced in the outer

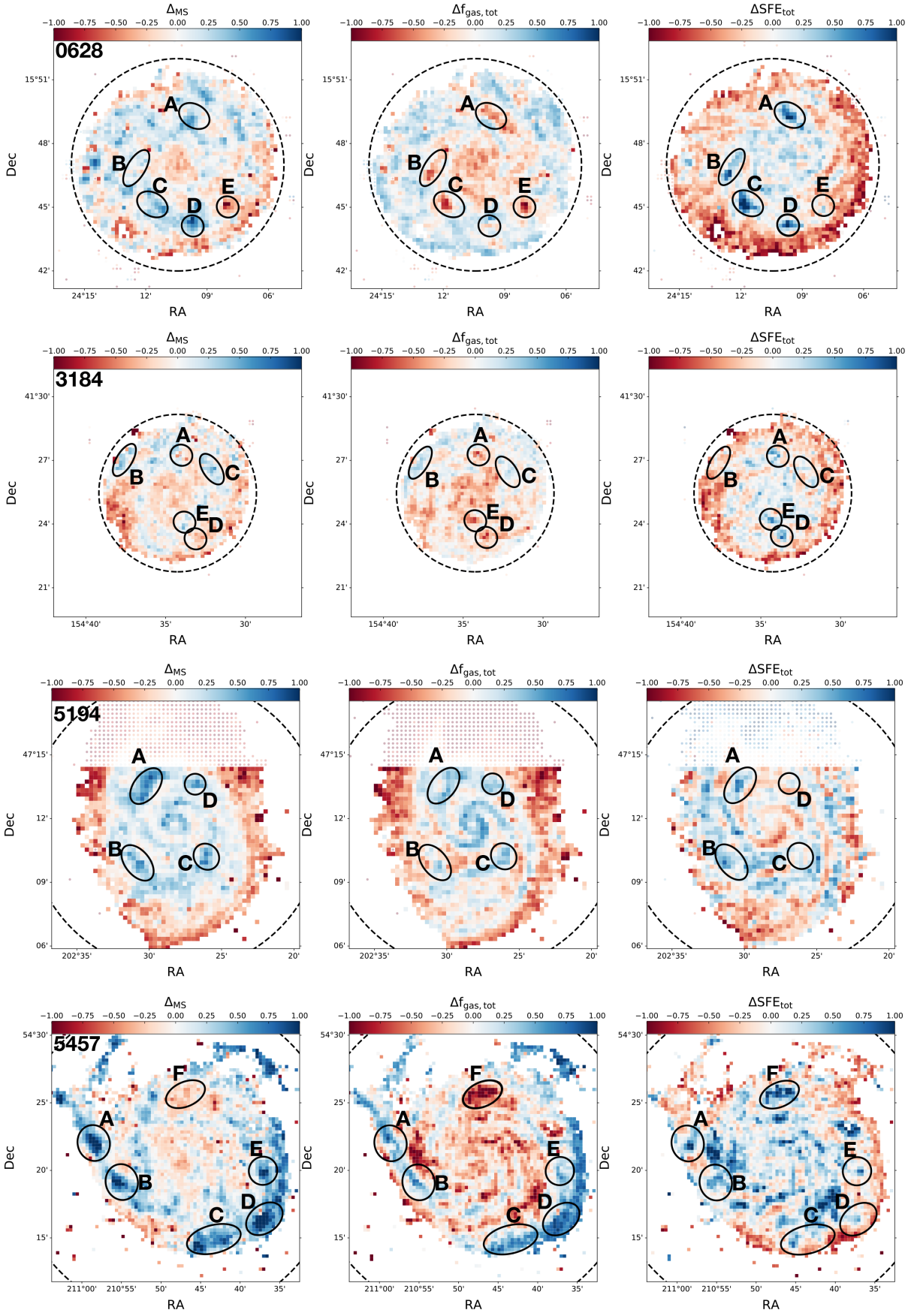

Figure B1. Δ_{MS} (left), $\Delta_{f_{gas,tot}}$ (centre), and $\Delta_{SFE,tot}$ (right) maps of (from top to bottom) NGC 0628, NGC 3184, NGC 5194, and NGC 5457. The highlighted regions are discussed more in detail in the text.

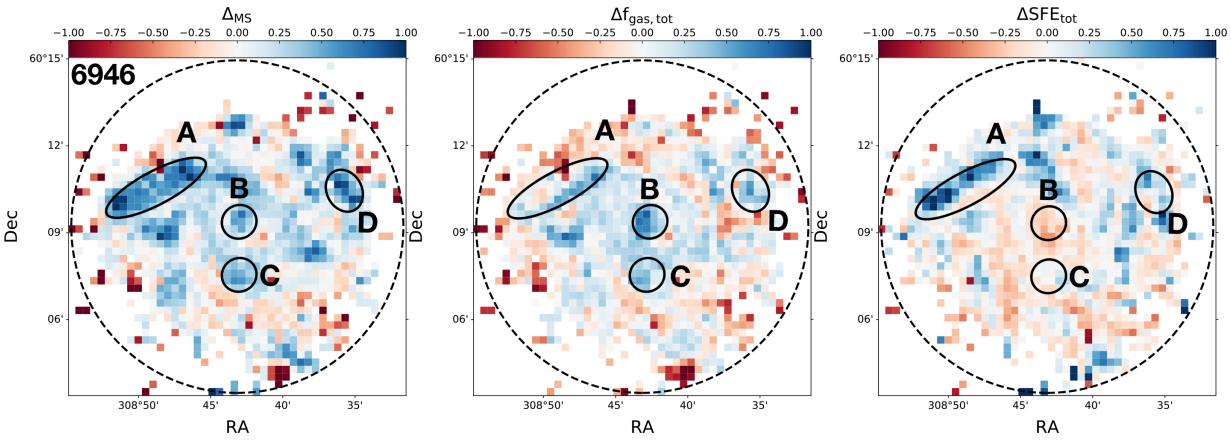

Figure B2. Δ_{MS} (left), $\Delta_{f_{gas,tot}}$ (centre), and $\Delta_{SFE,tot}$ (right) maps of NGC 6946. The highlighted regions are discussed more in detail in the text.

discs. Below we describe a few selected regions in each galaxy more in detail:

(i) The central region of NGC 0628, i.e. the bulge, is located below the MS and has low gas content, while $\Delta_{SFE,tot}$ varies of ± 0.3 dex around zero. Regions located in the upper envelope of the MS relation are located mostly along the spiral arms. We observe regions where $\Delta_{MS} \sim 0$ (A, B, and C) or $\Delta_{MS} \sim 1$ (D), or $\Delta_{MS} \sim -1$ (E), all with low gas fractions and high or average SFE.

(ii) NGC 3184 also has a central region characterized by mostly negative Δ_{MS} and $\Delta_{f_{gas,tot}}$, while $\Delta_{SFE,tot}$ is, for the majority of cells, positive. In the spiral arms, we observe regions where the SFR is significantly higher than the MS value (B and C) that correspond to gas fractions above the average, and varying SFE. We identify three blobs (A, D, and E) with negative $\Delta_{f_{gas,tot}}$ and Δ_{MS} varying slightly around the MS value (as in A and E) or $\Delta_{MS} < 0$ (as in D).

(iii) NGC 5194 is characterized by a central region that has SFR values mostly above the MS. Positive values of Δ_{MS} are located mainly along the spiral arms that are also well traced by an excess of total gas compared to the average. The regions A, B, C, and D are all above the MS relation, but they show different properties: while the majority of pixels within C and D are have $\Delta_{f_{gas,tot}} > 0$ and $\Delta_{SFE,tot} \sim 0$, A and B show clumps of $\Delta_{SFE,tot}$ well above 0 and $\Delta_{f_{gas,tot}}$ varying between negative and positive values.

(iv) NGC 5457 is characterized by two strong spiral arms with several blobs that have an SFR higher than the MS value (regions A, B, C, D, E). Within these regions, we observe gas fractions that are almost always higher than the MS values, while $\Delta_{SFE,tot}$ varies more strongly between positive and negative values. Region F, for which the majority of cells are well below the MS relation, has $\Delta_{SFE,tot} \sim 1$, but $\Delta_{f_{gas,tot}} \sim -1$.

(v) NGC 6946 has a central region characterized by SFR higher than MS values, high gas content and SFE lower than the average (region B). Regions A, C, and D are also characterized by values of Δ_{MS} close to 1, but different SFE. While regions A and D have close to normal gas content and SFE above the average, the more central regions B and C have a high gas content but a low SFE.

In general, we conclude that in the innermost and outer regions the decrease or enhancement of the local gas content follows closely that of the star formation rate along the MS. For the innermost region and the spiral arms, the enhancement or decrease of the SFE is opposite to that of the local gas content. But there are exceptions to this behaviour. Given the possible temporal and spatial lag between molecular and FUV peaks (Kruijssen et al. 2019), the relation between $\Delta_{SFE,tot}$ and Δ_{MS} for individual galaxies is more complex and requires dedicated analysis.

This paper has been typeset from a TEX/LATEX file prepared by the author.